Characteristics of cloud size of deep convection simulated by a global cloud resolving model

T. Inoue[1], M. Satoh[1, 2], H. Miura[2], B. Mapes[3]

1) Center for Climate System Research, University of Tokyo, 5-1-5 Kashiwanoha, Kashiwa-shi, Chiba, 277-8568, Japan

2) Frontier Research Center for Global Change, Japan Agency for Marine-Earth Science and Technology, 3173-25 Showa-machi,Kanazawa-ku,Yokohama-shi, Kanagawa,236-0001,Japan

3) Rosenstiel School of Marine and Atmospheric Sciences, University of Miami, Miami, FL, USA

4 Oct. 2007, submitted to *J. Meteor. Soc. Japan, Special Issue*

Corresponding author address:
Toshiro Inoue, toshiro@ccsr.u-tokyo.ac.jp

Abstract

Cloud size distributions of cloud cluster are analyzed for global cloud resolving simulations with the global nonhydrostatic model NICAM whose mesh interval is about 3.5km and 7km. The 3.5km-mesh simulation is performed for 7 days started at 00 UTC 25 Dec 2006 by giving an initial condition of reanalysis data, while the 7km-mesh simulation is run for 32 days from 00 UTC 15 Dec 2006. We used outgoing long-wave radiation (OLR) simulated by NICAM to calculate size distributions of deep convection, and compared with those analyzed using equivalent blackbody temperature (T_{BB}) of the infrared channel of 11 μm of the Japanese geostationary meteorological satellite (MTSAT-1R). We select two threshold temperatures, 208 K and 253 K, to identify deep convective areas including anvil cloud. Specifically, we call clouds defined by the 208 K-threshold "deeper" convective clouds. Over the tropical region covering the maritime continent and the western tropical Pacific ocean (10S-10N, 90E-160W), we examined size of cloud areas defined by the two T_{BB} threshold values and corresponding threshold values of OLR, which were chosen by comparing cumulative histograms of T_{BB} and OLR in this region.

Resolution dependency by NICAM shows that the overall cloud size distribution of the 3.5 km-mesh simulation is much closer to that of the MTSAT-1R observation than that of the 7 km-mesh simulation. Size distributions of deep convection in both simulations indicate nearly lognormal as is seen in the satellite observations. The 3.5 km-mesh simulation shows slightly less

frequency than the MTSAT-1R observation for smaller size of deeper convection, and it does not reproduce very large clouds. When compared cloud characteristics over land and ocean, simulated cloud size statistics are closer to the satellite observation in the maritime continent region (westward of 160E) than in the open ocean region (eastward of 160E). Comparison of temporal variation of cloud area shows that the 3.5 km-mesh simulation captures clear signals of diurnal cycles both over the maritime continent and the open ocean regions, together with amplification associated with the MJO event. Morning and afternoon difference of convective activity over large island within the maritime continent is also simulated by 3.5km-mesh simulation.

When one uses a global cloud resolving model for climate studies, the analysis of cloud size distributions gives another dimension to improve cloud properties of simulations. It is not only relevant to realistic representations of deep convection, but is also useful for improving the energy budget of global cloud resolving simulations.

1. Introduction

Recently, simulations of a global cloud resolving model are becoming available using an enormous computer power (Tomita et al, 2005; Satoh et al, 2005). A global cloud resolving model (GCRM), which is defined here as a global nonhydrostatic model with mesh size of about a few kilometers and uses explicit cloud process without cumulus parameterizations, simultaneously calculate meso-scale circulations associated with deep convection and large-scale circulations driven by organized convection. As an organized structure of meso-scale circulations, cloud clusters are naturally resolved in these simulations (Nasuno et al., 2007), while they are not simulated well by traditional general circulation models (GCMs) with cumulus parameterizations. Simulations with GCRM enable us to discuss realisms of cloud characteristics, particularly those of cloud clusters whose scale is a few hundreds of kilometers. At this new stage of high-resolution global atmospheric modeling, we can analyze numerically simulated data with GCRM using the methods used for geostationary meteorological satellite (GMS) observations, whose resolution is comparable to the mesh size of GCRM.

Analysis of cloud clusters using the GMS observations has a long history (e.g., Chang, 1970; Nakazawa 1988; Mapes and House 1993). To identify deep clouds, appropriate values of equivalent blackbody temperature (T_{BB}) of infrared data are used. Convective clouds over the tropics have a spectrum in size ranging from small isolated cumulus to large convective clusters. These

convective clouds affect the vertical distribution of heating in the troposphere and radiation budget as well. Size distributions and temporal evolutions of deep convection have been studied using satellite observation data (e.g., Williams and Houze 1987; Mapes and Houze 1993; Machado et al 1993). Methods to analyze spatial and temporal variations of deep convection defined by infrared data can be used for simulated data with GCRM, because both data are provided by a few kilometer-interval. Similar analysis methods could be used for data produced by traditional GCMs, but direct comparison cannot be made because of the gap of the resolutions between GCMs and observations.

Using GCRM data, we obtain statistical properties of cloud and precipitation systems similar to those retrieved from satellite observations. Satoh et al.(2007b) showed the statistics of the precipitation height for the aqua planet experiment with GCRM (Tomita et al. 2005; Satoh et al. 2005) and compared with those of the Precipitation Radar (PR) on board Tropical Rainfall Measurement Mission (TRMM) (Takayabu 2002). It was found that the frequency of the precipitation top height of convective rains with GCRM has profiles similar to the satellite observations at least qualitatively. However, since the simulation was idealized one under the aqua planet condition, the comparison was limited to statistics over wide domain of ocean in general and it was difficult to identify cause of the discrepancies.

Recently, simulations with GCRM under more realistic conditions with land and sea distributions

have been performed (Miura et al., 2007a, 2007b). Giving initial fields interpolated using reanalysis data, they integrated the Nonhydrostatic ICosahedral Atmospheric Model (NICAM) for one month with the mesh interval of about 7 km and for one week with mesh interval of about 3.5 km at highest resolution. Miura et al. (2007b) captured realistic behaviors of a Madden-Julian Oscillation event seen in the observation; slowly eastward propagation of cloud systems is reproduced and fine scale structure within the MJO is resolved. In this simulation, not only large-scale organized cloud systems associated with the MJO, but cloud clusters whose size is about hundreds kilometers are also simulated. Figure 1 compares the cloud distribution of the Japanese geostationary meteorological satellite of Multi-functional Transport Satellite (MTSAT-1R) observation and that of the NICAM simulation at 00 UTC 26 Dec 2006 over the western tropical Pacific ocean covering the maritime continent: T_{BB} colder than 253 K is shown for the infrared image of MTSAT-1R, while the outgoing longwave radiation OLR lower than 210 W m^{-2} is shown for the NICAM simulation with about 3.5 km-mesh size (DX3.5km). This shows sizes and locations of cloud clusters are realistically simulated, particularly over the maritime continent and the ITCZ region over the ocean between 160E-160W.

In the present study, we analyze deep convective clouds over the western tropical Pacific using the simulated data by NICAM shown above (Miura et al., 2007b). Cloud size distribution by NICAM is compared with those analyzed by using T_{BB} of MTSAT-1R. From this comparison, we will argue

quantitatively how cloud clusters of the model simulation are comparable to those of the observations. We will investigate the dependency on the model resolution, and contrast between the maritime continent and the open ocean regions, together with temporal variations. Since OLR is directly related to the energy transfer, this analysis is useful to investigate the energy budget of the model. In section 2, we will describe the experimental setting, and the analysis method is described in section 3. Results are shown in section 4, and summary and discussion are followed in the final section.

2. Experimental design

We used the NICAM for global cloud resolving simulations (Tomita and Satoh 2004; Satoh et al.2007a). The mesh size is about 7 km and 3.5 km, which correspond to the recursive grid-division level 10 and 11, respectively (Tomita et al., 2001; 2002). The 3.5km-mesh simulation was started at 00 UTC 25 Dec 2006 and integrated for 7 days, while the 7km-mesh simulation was started at 00 UTC 15 Dec 2006 and integrated for 32days to study the whole cycle of the MJO event (Miura et al., 2007b). These simulations will be denoted by DX3.5km and DX7km, respectively. The computation was performed using the Earth Simulator. All the physical schemes are the same regardless of the resolutions. No cumulus parameterization was used, and explicit cloud physics scheme of Grabowski (1998) is used. The boundary layer scheme based on Mellor and Yamada

level 2 with moist process is implemented (Yamada and Mellor, 1979; Nakanishi and Niino 2004). The radiation scheme MSTRNX (Nakajima et al. 2000; Sekiguchi , 2004) is called every 5 minutes. We use 40 levels in the vertical with thinner depths near the surface. The time step interval is 20 sec for DX7km, and 15 sec for DX3.5km.

The data was stored in 90 min interval. The original icosahedral grid data were converted to the longitude-latitude grid by bi-linear interpolation. The numbers of grid points along the equator are 10,240 and 5,120 for DX3.5km and DX7km, respectively, so that the typical grid intervals are 3.9 km and 7.8 km, respectively. Note that the resolution of the infrared data of MTSAT-1R is provided by 0.05 deg interval, which is almost comparable to the grid interval of DX3.5km.

3. Data and analysis

In this study, we focus on evaluations of deep convection simulated by NICAM over the western tropical Pacific ocean. Simulated upwelling longwave radiation (OLR) by NICAM is compared with T_{BB} observed by MTSAT-1R. The target area of our study is confined over the maritime continent region of 10S-10N and 90E-160E and the open ocean area of 10S-10N and 160E-160W. The brightness temperatures of 208 K and 253 K are used to define deep convective areas associated with anvil. We specifically call clouds defined by the 208 K threshold “deeper” convective clouds. The 208 K T_{BB} threshold value is selected considering the study by Mapes and

Houze (1993). Machado et al. (1993) used the 253 K threshold as the largest T_{BB} to define deep convective clouds. The temperature 253 K corresponds to about 7.9 km height (400 hPa) in the US tropical standard atmosphere. Although OLR and T_{BB} are different physical parameters, we can see the similarity of distribution patterns associated with deep convection. Inoue and Ackerman (2002) studied the OLR in terms of cloud types. Inoue et al. (2006) showed the conventional OLR threshold to define deep convection corresponds to the optically thicker cirrus type cloud rather than cumulonimbus type cloud. Cumulative distributions of T_{BB} and OLR are used to bridge between the two parameters. The corresponding OLR values for the T_{BB} threshold values are determined by comparing the cumulative distributions of T_{BB} and OLR.

Figure 2 shows cumulative distributions of T_{BB} observed by MTSAT-1R (a) and OLR simulated by NICAM (b) over the area of 10S-10N and 90E-160W during 26-31 Dec 2006. In Fig. 2(b), cumulative distributions of both the 3.5km and 7km NICAM simulations (DX3.5km, DX7km) are shown. The arrows show the cumulative percentage corresponding to 208 K and 253 K T_{BB} in (a) and corresponding OLR values in (b). The cumulative percentages of T_{BB} corresponding to the 208 K and 253 K thresholds are 3 % and 32 % in Fig. 2(a). The equivalent OLR to the T_{BB} threshold is determined from the cumulative distributions of OLR over the same area and period. The corresponding OLR values to 208 K and 253 K in DX3.5km are 90 W m^{-2} and 210 W m^{-2}, respectively. For DX7km, we used the same OLR threshold values 90 W m^{-2} and 210 W m^{-2} in

spite that the cumulative distribution is slightly different from that of DX3.5km. Using the above thresholds, we studied characteristics of deep/deeper convective clouds simulated by NICAM comparing with the satellite observation over the tropical western Pacific ocean of 10S-10N and 90E-160W.

4. Results

a) Cloud size of deep convection

Cloud size of deep convection is defined as contiguous regions of T_{BB} colder than the threshold values for infrared image of the satellite observations and those of OLR smaller than the corresponding threshold values for NICAM simulations. Figure 3 is symbolic representation of deep convection regions by circle for 00 UTC 26 Dec 2006. Cloud areas colder than 253 K by the MTSAT-1R observation and deep convective areas of OLR less than 210 W m^{-2} by the NICAM DX3.5km and DX7km simulation are shown in (a), (b), and (c), respectively. The size of a circle represents the size of a contiguous region of clouds and the center of the circle is located at the areal center of the contiguous cloud region. Note that circles are depicted only for deep convection regions whose centers are located within the analysis domain (10S-10N, 90E-160W). The same scale is used for these three figures. The area coverage over 10S-10N and 90E-160W in this case are 5.8×10^6 , 9.1×10^6, and 8.4×10^6 km^2 in total and 2.8×10^3, 5.1×10^3, and 8.7×10^3 km^2 as

average, respectively. The maximum size is 5.8×10^5, 4.2×10^5 and 3.2×10^5 km^2 and the number of deep convective clouds is 2107, 1790 and 973, respectively. As seen from Fig. 3, the largest size of cloud clusters appeared in the MTSAT-1R infrared images, while there are more large clouds appeared in both NICAM DX3.5km and DX7km simulations at this time.

Similar analysis for the deeper convective area defined by 208 K threshold (not shown) indicated that the area coverage over 10S-10N and 90E-160W are 6.3×10^5, 7.3×10^5 and 3.7×10^5 km^2 in total and 1.8×10^3, 1.5×10^3, and 4.5×10^3 km^2 as average, respectively, for MTSAT-1R, DX3.km and DX7km, respectively. The maximum size is 8.4×10^4, 4.1×10^4 and 6.0×10^4 km^2 and the number of cloud clusters is 357, 485, and 85, respectively. Again, the largest size of deep convection is observed in the satellite analysis. The mean size of deep convection is larger in DX7km than DX3.5km, while numbers of deeper/deep convection are smaller in DX7km than in DX3.5km for both thresholds.

Size distributions of deeper convection defined by T_{BB} = 208 K and OLR = 90 W m^{-2} are shown in Fig. 4 and 5. Figure 4 shows histograms of the size dimension (square root of area) in km, while Fig. 5 is cumulative distribution functions with log scale for cloud area. Figure 4 also shows histograms of less deeper convection defined by T_{BB} = 253 K and OLR = 210 W m^{-2} (bottom). Each data appears a straight line in Fig.5; therefore, cloud size is log-normally distributed for both simulations and satellite observation. The size of deeper convection of DX3km is much closer to

that of MTSAT-1R than that of DX7km. These figures also indicate that the size of deeper convection of DX7km is larger than that of DX3.5km and MTSAT-1R. The size of deeper convection of MTSAT-1R becomes more frequent for the size larger than 5000 km^2 compared with that of DX3.5km. On the other hand, smaller size of deeper convection is less frequently observed by DX3.5km than MTSAT-1R. This implies that the smaller clouds marginally resolved by MTSAT-1R cannot be simulated well by DX3.5km as seen in relative size distribution.

Contrasting feature of cloud clusters between the maritime continent and the open ocean is examined using the size distributions of deep/deeper convection. Figure 6 shows the contrast of size distribution over the maritime continent and over the open ocean for the 208 K threshold (a) and 253 K threshold (b). The satellite observation indicates cloud size is slightly larger over the maritime continent region than the open ocean region for both the 208 K and 253 K thresholds. However, the larger cloud area appears more frequently over the open ocean region than over the maritime continent region for the 208 K threshold. This tendency is not clear for the 253 K threshold.

Figure 7 shows the contrast of size distributions over the maritime continent and the open ocean regions for the 90 W m^{-2} threshold (a) and the 210 W m^{-2} threshold (b) in the NICAM DX3.5km simulation. The cloud size is larger over the maritime continent region than over the open ocean region. This tendency is consistent with the satellite observation, although the difference is slightly

enhanced in DX3.5km. However, contrary to the satellite observation, the larger clouds are simulated more over the maritime continent region for the 210 W m^{-2} threshold.

Comparisons between the NICAM simulation and the satellite observation over the both regions are shown in Fig. 8 and 9, which can be reproduced from Fig. 6 and 7. The deeper clouds (defined by the 208 K and 90 W m^{-2} thresholds) are compared in Fig. 8 over the maritime continent (a) and over the open ocean (b). The size distribution is generally similar for both the regions. The number of clouds smaller than 7×10^3 km^2 is less frequent in DX3.5km both over the maritime continent and the open ocean regions. The difference for larger clouds is more clearly seen over the open ocean region, although the number of such large clouds is small. This suggests the NICAM DX3.5km simulation has deficiency in depicting larger clouds of deeper convection both over the maritime continent and the open ocean regions. The deeper convection is related to cores of deep cumulonimbus, It is difficult to underpin the reasons for this discrepancy only from the present analysis. We speculate that detrainment process near the tropopause might not be represented well by the simulation due to insufficient vertical resolution near the tropopause transition layer. We note that cloud amount in the core of deep convection is also related to cloud microphysics schemes through precipitation efficiency (Sui et al. 2005).

Figure 9 is the comparison of less deeper convective clouds defined by the 253 K and 210 W m^{-2} thresholds. The cloud size of DX3.5km is wider than that of MTSAT-1R over both regions. This

suggests that the cloud areas define by OLR = 210 W m^{-2} (T_{BB} = 253 K) is overestimated by DX3.5km. Figure 10 shows the cloud type map constructed from the split window method (Inoue, 1987) at 00 UTC 26 Dec 2006. The brightness temperature difference between the split window, BTD=T_{BB}(11μm) - T_{BB}(12μm), indicates optical thickness. BTD is larger for optically thinner clouds, while BTD becomes zero for black-body clouds. In Fig.10, we select 0.5 K threshold to classify optically thick/thinner clouds. Clouds shown in the figure are all colder than 253 K. Clouds colored in purple, blue, and green correspond to clouds colder than 208 K, optically thick clouds, and optically thinner clouds, respectively. As seen in the figure, larger clouds those of T_{BB} between 208 K and 253 K are mostly optically thinner cloud (green in the figure), while smaller clouds are mostly optically thick cloud (blue in the figure). Further, most of these optically thinner clouds are surrounding the clouds colder than 208 K (purple in the Fig. 10) over the 10S-10N area. Therefore, this larger size of deep convective cloud areas corresponds to optically thinner clouds. The size of clouds defined by the 253 K threshold is generally smaller than those of the DX3.5km simulation (Figs 3 and 9); this implies that the NICAM DX3.5km simulation overestimates optically thinner clouds such as cirrus anvil. The representation of cirrus anvil is sensitive to details of cloud microphysics (Iga et al. 2007).

b) Temporal variations of cloud size

Figure 11 shows temporal variations of the total area of deep convection defined by the 208 K, 90 W m^{-2} thresholds over the maritime continent region (a) and the open ocean region (b) during 00 UTC 26 Dec 2006 and 00 UTC 1 Jan 2007. In this figure, cloud areas whose center located within the boundary are all counted. The total size of deep convection simulated by DX3.5km and DX7km are generally smaller than the satellite observations. However, the phase of the temporal variation observed by satellite is well depicted by DX3.5km except for the first few days of the simulation. DX7km simulation cannot capture the characteristics of this temporal variation and the amplitude is generally smaller than that of DX3.5km.

The simulated temporal variation by DX3.5km is more evident when the thresholds are changed to 253 K and 210 W m^{-2} as shown by Fig. 12. The DX7km simulation captures some signal of the temporal variation observed by satellite over the maritime continent region, although it has systematic time lag in phase. The temporal variation of deep convective cloud area both over the maritime continent and the open ocean regions is reasonably represented by the NICAM DX3.5km simulation, although not well represented by the NICAM DX7km simulation.

Diurnal variation of deep convection has been studied over this area using the infrared data of GMS and the PR data of TRMM(e.g. Murakami 1983; Ichikawa and Yasunari, 2006; Takayabu, 2002). It has been shown that the maximum activity of deep convection appears late afternoon over the land area, and early morning over the ocean area. In the present study, we define the two areas

of the maritime continent region and the open ocean region with relatively larger longitudinal area, so that there is some time lag in identifying local time. Further, the MJO could modulate the diurnal variation of convective activity (Tian et al, 2006; Ichiwaka and Yasunari 2007). However, as is seen in Fig.11(a), the satellite observation suggests the early morning maximum (21 UTC; 5 LT) in convective activity over the maritime continent region. This phase is not consistent with previous studies, however, we can see clear diurnal signal during this specific period and relatively larger area in the satellite observation (red curve in Fig. 11(a)). The NICAM DX3.5km simulation depicts this diurnal variation, although the peak of convective activity appears about 3 hours later (although 9 hours on 27 Dec), while the maximum convective activity over the open ocean region is seen during 18-21 UTC (5-8 LT) in the satellite observation (not clear on 29 Dec). The time of the peak of deep convection activity during this period is slightly later than previous studies. The temporal variation of deep convection defined by the 208 K threshold is generally represented by DX3.5km including the diurnal variation. The correlation coefficient between DX3.5km and satellite observation is 0.62 for Fig. 11(a), although 0.13 for Fig. 11(b). However, the DX7km simulation cannot represent the temporal variation appeared in the satellite observation.

As is seen in Fig.12, the diurnal variation of deep convection defined by 210 W m^{-2} over the maritime continent region corresponds well to that of the satellite observation, considering the time lag. The peak time of cloud area appears 9 UTC (17 LT) over the maritime continent region, while

that over the open ocean region appears about 6 UTC (17 LT). The correlation coefficient between DX3.5km and the satellite observation is 0.82 for Fig. 12(a) and 0.54 for Fig. 12(b). The time lag between the peak of deeper convective cloud area colder than 208 K and that of cloud area colder than 253 K is about 12 hours both over the maritime continent and the open ocean regions. The similar time lag is shown in Machado et al. (1993). They studied 15 large cloud clusters and found that the time lag between the peak of cloud cluster size defined by 207 K threshold and 253 K threshold was 12 hours. They conclude this time lag is a reflection of development of cloud cluster and merge into larger clusters.

Mapes and Houze (1993) discussed the morning and afternoon difference of deep convection using GMS data. They showed clear difference of convective activity between morning and afternoon over large island in the maritime continent for the cloud clusters of 1,000-3,000 km^2. in size although they showed no difference for cloud clusters larger than 30,000 km^2. Figure 13 shows the geographical distribution of deep convection defined by the 208K threshold at 00 UTC and 09 UTC composite of 6 days during 26 Dec and 31 Dec 2006. Over the large islands of the maritime continent (New-Guinea, Borneo, and Sumatra), there are almost no deep clouds at 00 UTC (about 8 LT), while deep convection becomes active at 09 UTC (about 17 LT). Over the open ocean region, on the other hand, deep convection is more active at 00 UTC (about 11 LT) than at 09 UTC (about 20 LT). This feature is consistent with the previous studies. Figure 14 shows the geographical

distribution of deep convection defined by the 90 W m^{-2} threshold in the NICAM DX3.5km simulation for 00 UTC and 09 UTC. The DX3.5km simulation represents similar characteristics of deep convective activity. The deep convection over the large islands of the maritime continent is less active at 00 UTC (about 8 LT) and enhanced at 09 UTC (17 LT). The deep convection over the open ocean region is more active at 00 UTC (about 11 LT) than 09 UTC (about 20 LT).

5. Summary and discussion

We have compared the size distributions of deep convection between the global cloud resolving simulations by NICAM and the satellite observations by MTSAT-1R. The numerically simulated data by NICAM with the mesh-size of 3.5 km (DX3.5km) and 7 km (DX7km) from 00 UTC 26 Dec 2006 to 00 UTC 1 Jan 2007 were used for the analysis. To define deep convection, we first determine threshold values of the outgoing longwave radiation (OLR) corresponding to the equivalent blackbody temperature T_{BB} of the infrared channel of the satellite observations using the cumulative distribution functions of T_{BB} and OLR. The contiguous cloud areas are calculated by using these thresholds both for the NICAM simulations and the MTSAT-1R observations.

The size distribution of deep convective clouds simulated by both DX3.5km and DX7km indicates log-normal distribution as is seen in the satellite data. In general, the size distribution of DX3.5km is much closer to that of the satellite observations than that of DX7km. In details,

DX3.5km has less frequency in clouds smaller than 5×10^3 km than the satellite observations. This comes from the fact that DX3.5km cannot resolve very small clouds comparable to grid scales. From the split window analysis based on Inoue (1987), it was found that these small clouds are mostly optically thick and could be categorized as cumulus congestus clouds. Size distributions over the maritime continent and the open ocean are basically similar, but the larger clouds in the maritime continent are represented better than in the open ocean. This is because the convection in the maritime continent is stronger than the open ocean due to the diurnal cycle caused by the land surface heating.

To examine the diurnal cycle of deep convection, the temporal variations of the total cloud area are analyzed over the maritime continent and the open ocean regions. NICAM captured the diurnal variations of the total cloud area very well particularly over the maritime continent region. The peak times of the cloud size are different between the cases when the 208 K and 235 K thresholds are used. The time lag is about 12 hours both for MTSAT-1R and DX3.5km; this suggests that the spread of anvil cloud from the core of deep convection or merge of cloud clusters is well represented by DX3.5km.

The size distribution analysis of cloud clusters presented in this study has following importance. First, we can evaluate quantitatively the difference and the realism of clouds simulated by the global cloud resolving simulations. We have compared the size and the temporal variation of deep

convective clouds to understand the behaviors of the model simulations. From these results, we will have a guidance to improve model simulations. For example, the present analysis showed that NICAM has less frequency in grid-scale small clouds. These clouds are categorized as cumulus congestus using the split window analysis. This result suggests that the temporal variation of individual cumulus convection is not well represented by the model. It will be a future task to examine how the evolution of each cumulus affects simulations of successive cloud clusters. We examined cloud characteristics over the western tropical Pacific ocean covering the maritime continent. Recently, it has been realized that more realistic representation of convection over the maritime continent is one of the major challenges to global atmospheric modeling because of its complex system of islands and oceans (e.g. Neale and Slingo, 2003). Here, we examine overall behaviors of deep convection simulated by a global cloud resolving model in a statistical sense using cloud size distributions analysis. We will further proceed to detailed comparisons of individual convective events.

Second, the energy budget of the global cloud resolving simulations are directly affected by the size of deep convection, i.e., the coverage of anvil clouds. It is also very sensitive to the cloud microphysical processes used in the model. We can evaluate the cloud microphysical processes in terms of the energy budget through the size of upper clouds. Figure 15 is the latitudinal distributions of OLR for DX3.5km and DX7km of the NICAM simulations between 90E-160W

and compares with the observed OLR by the NOAA interpolated OLR data (National Oceanic and Atmospheric Administration). This shows that the simulated values of OLR are closer to the observation over the equatorial cloud areas, although higher bias is seen in the sub-tropics and higher-latitudes. It should be noted that since this simulation is intended for short duration for a few weeks, the bias in OLR does not affects the main results of the present analysis. Here, we concentrate on the equatorial region between 10S-10N. From Fig. 15, the regional mean OLR is very similar between DX3.5km and DX7km, so it is hard to evaluate the simulated results only from the averaged OLR. By further analyzing the size of deep convective clouds as shown in the present study, we have clarified the resolution dependency. This analysis will be useful to improve models; if we change parameters in physical processes such as cloud microphysics and boundary schemes, OLR would change (Iga et al. 2007); the size of clouds will provide another dimension to improve performance of global high-resolution models.

Acknowledgment

Numerical experiments of NICAM were done using the Earth Simulator. This research was supported by Core Research for Evolutional Science and Technology, Japan Science and Technology Agency (CREST,JST). We also thank members of the NICAM team: Hirofumi Tomita, Tomoe Nasuno, Shin-ichi Iga, Akira Noda, Wataru Yanase, and Kazuyoshi Oouchi.

References

Chang, C.-P., 1970: Westward Propagating Cloud Patterns in the Tropical Pacific as seen from Time-Composite Satellite Photographs. *J. Atmos. Sci*., **27**, 133-138.

Grabowski, W.W., 1998: Toward cloud resolving modeling of large-scale tropical circulations: A simple cloud microphysics parameterization. *J. Atmos. Sci.*, **55**, 3283-3298.

Ichikawa, H. and T. Yasunari, 2006: Time-space characteristics of diurnal rainfall over Borneo and surrounding oceans as observed by TRMM-PR. *J. Cimate*, **19**, 1238-1260.

Ichikawa, H., Yasunari, T., 2007: Propagating diurnal disturbances embedded in the Madden-Julian Oscillation. *Geophys. Res. Lett.*, 34, L18811, doi:10.1029/2007GL030480

Iga, S., H. Tomita, Y. Tsushima, and M. Satoh, 2007: Climatology of a nonhydrostatic global model with explicit cloud processes. *Geophys. Res. Lett.*, in the press.

Inoue, T., 1987: A cloud type classification with NOAA 7 Split-Window measurements. *J. Geophys. Res.*, **92**, 3991-4000.

Inoue, T. and S. Ackerman, 2002: Radiative effect of various cloud types as classified by the split window technique over the eastern sub-tropical Pacific derived from collocated ERBE and AVHRR data. J. Meteor. Soc. Japan, J. Meteor. Soc. Japan, 80, 1383-1394.

Inoue, T., H. Ueda and T. Inoue, 2006: Cloud properties over the Bay of Bengal derived from

NOAA-9 split window data and TRMM PR rainfall product. SOLA, 2, 41-44.

Machado, L. A., J-Ph. Duvel, and M. Desbois, 1993: Diurnal variation and modulation by easterly waves of the size distribution of convective cloud clusters over west Africa and Atlantic Ocean. *Mon. Wea. Rev.*, **121**, 37-49.

Mapes,B.E. and House,Jr.R. A., 1993: Cloud clusters and superclusters over the oceanic warm pool. *Mon. Wea. Rev.*, **121**, 1398-1416.

Miura, H., Masaki Satoh, Hirofumi Tomita, Tomoe Nasuno, Shin-ichi Iga, and Akira T. Noda, 2007a: A short-duration global cloud-resolving simulation with a realistic land and sea distribution. *Geophys. Res. Lett.*, **34**, L02804, doi:10.1029/2006GL027448.

Miura, H., Satoh. M., Nasuno, T., Noda, A.T., Oouchi, K, 2007b: An Madden-Julian Oscillation event realistically simulated by a global cloud-resolving model, submitted.

Murakami, M., 1983; Analysis of deep convective activity over the western Pacific and Southern Asia. *J. Meteor. Soc. Japan*, **61**, 60-75.

Neale, R. and Slingo, J., 2003: The Maritime Continent and Its Role in the Global Climate: A GCM Study. *J. Clim.*, 16, 834-848.

Nakanishi, M. and Niino, H., 2004: Am improved Mellor-Yamada Level-3 model with condensation physics: its design and verification. *Boundary-Layer Meteor*., **112**, 1-31.

Nakajima,T., Tsukamoto,M., Tsushima.Y., Numaguti,A., Kimura,T., 2000: Modeling of the

radiative process in an atmospheric general circulation model. *Applied Optics*, **39**, 4869-4878.

Nakazawa, T., 1988: Tropical superclusters within intraseasonal variations over the western Pacific. *J. Meteor. Soc. Japan*, **66**, 823-839.

Nasuno,T., Tomita,H., Iga,S., Miura,H., Satoh,M., 2007: Multi-scale organization of convection simulated with explicit cloud processes on an aquaplanet. *J. Atmos. Sci.*, **64**, 1902-1921.

Satoh,M., Tomita, H, Miura, H., Iga, S., and Nasuno, T., 2005: Development of a global cloud resolving model - a multi-scale structure of tropical convections -. *J. Earth Simulator*, **3**, 11-19.

Satoh, M., T. Matsuno,T., H. Tomita, H. Miura, T. Nasuno, S. Iga, 2007a: Nonhydrostatic Icosahedral Atmospheric Model (NICAM) for global cloud resolving simulations. *J. Comp. Phys.*, doi:10.1016/j.jcp.2007.02.006.

Satoh, M., T. Nasuno, H. Miura, H. Tomita, S. Iga, Y. Takayabu, 2007b: Precipitation statistics comparison between global cloud resolving simulation with NICAM and TRMM PR data. In "High Resolution Numerical Modelling of the Atmosphere and Ocean" edited by Wataru Ohfuchi and Kevin Hamilton. ISBN: 978-0387366715, 280pp.

Sekiguchi, M. , 2004: A study on evaluation of the radiative flux and its computational optimization in the gaseous absorbing atmosphere. Ph.D. dissertation, University of Tokyo, 121 pp. (Japanese).

Sui,C.-H., Li, X., Yang, M.-J., Huang,H.-L., 2005: Estimation of oceanic precipitation efficiency in

cloud models. *J. Atmos. Sci.*, 62, 4358-4370.

Takayabu, Y. N., 2002: Spectral representation of rain profiles and diurnal variations observed with TRMM PR over the equatorial area. *Geophys. Res. Lett.*, **29**, doi:10.1029/2001GL014113.

Tian B., D. E. Waliser, E. J. Fetzer, 2006: Modulation of the diurnal cycle of tropical deep convective clouds by the MJO, *Geophys. Res. Lett.*, **33**, L20704, doi:10.1029/2006GL027752.

Tomita,H., Tsugawa,M., Satoh,M., Goto, K., 2001: Shallow water model on a modified icosagedral geodesic grid by using spring dynamics. *J. Comp. Phys.*, **174**, 579-613

Tomita,H., Satoh,M., Goto, K., 2002: An optimization of icosahedral grid by using spring dynamics. *J. Comp. Phys.*, **183**, 307-331

Tomita,H. and Satoh,M., 2004: A new dynamical framework of nonhydrostatic global model using the icosahedral grid. *Fluid Dyn. Res.*, **34**, 357-400.

Tomita, H, Miura, H., Iga, S., Nasuno, T., and Satoh,M., 2005: A global cloud-resolving simulation: preliminary results from an aqua planet experiment. *Geophys. Res. Lett.*, **32**, L08805, doi:10.1029/2005GL022459.

Yamada T. and Mellor, G. L., 1979: A numerical simulation of BOMEX data using a turbulence closure model coupled with ensemble relations. *Quart. J. Roy. Met. Soc.*, **105**, 915-944. Williams, M., and R. A. Houze, Jr., 1987: Satellite-observed characteristics of winter monsoon cloud clusters. *Mon. Wea. Rev.*, **115**, 505-519.

Figure captions

Figure 1

Distributions of T_{BB} by MTSAT-1R (top) and OLR by DX3.5km of the NICAM simulation (bottom) at 00 UTC 26 Dec 2006. Only the areas with T_{BB} colder than 253 K and OLR lower than 210 W m^{-2} are shown for deep convection.

Figure 2

Cumulative distributions of T_{BB} observed by MTSAT-1R (a) and OLR simulated by NICAM (b) over the area of 10S-10N and 90E-160W during 26-29 Dec 2006.

Figure 3

Deep convection regions defined by 253K (210 W m^{-2}) are represented by circle for the satellite observation (top), DX3.5km of the NICAM simulation (middle) and DX7km of the NICAM simulation (bottom) at 00 UTC 26 Dec 2006.

Figure 4

Histograms of cloud size of T_{BB} and OLR for deep convection defined by the 208 K and 90 W m^{-2}

thresholds (top) and by the 253 K and 210 W m^{-2} thresholds (bottom) . The size in abscissa is defined as square of area (km^2).

Figure 5

Size distributions of T_{BB} and OLR for deep convection defined by 208 K and 90 W m^{-2}. Statistics are analyzed for data between 26 and 29 Dec 2006.

Figure 6

Size distributions of T_{BB} for deep convection defined by 208 K (a) and 253 K (b) for the satellite observation over the maritime continent and the open ocean regions.

Figure 7

Size distributions of OLR for deep convection defined by 90 W m^{-2} (a) and 210 W m^{-2} (b) for the NICAM DX3.5km simulation.

Figure 8

Size distributions of T_{BB} and OLR for deep convection defined by 208 K and 90 W m^{-2} over the maritime continent (a) and the open ocean (b).

Figure 9

Same as Fig. 8 except for T_{BB} and OLR for thresholds of 253 K and 210 W m^{-2}.

Figure 10

Cloud type map constructed from the split window method at 00 UTC 26 Dec 2006. Clouds colored in purple, blue, and green correspond to clouds colder than 208 K, optically thick clouds, and optically thin clouds colder than 253 K, respectively.

Figure 11

Temporal variations of the total area of deep convection defined by the 208 K and 90 W m^{-2} thresholds over the maritime continent (a) and the open ocean (b) during 00 UTC 26 and 21 UTC 29 Dec 2006.

Figure 12

Same as Fig.11 except for the 253 K and 210 W m^{-2} thresholds.

Figure 13

Geographical distribution of deep convection defined by 208K-threshold and size shown in color for MTSAT-1R observation at 00 UTC and 09 UTC.

Figure 14

Same as Fig. 13 except for the deep convection defined by 90 W m^{-2} thresholds.

Figure 15

Latitudinal distributions of OLR between 90E-160W for one-day average of 26 Dec 2006. Red curve is for DX3.5km, blue curve is for DX7km, and black curve is for the NOAA-interpolated OLR.

Figure 1

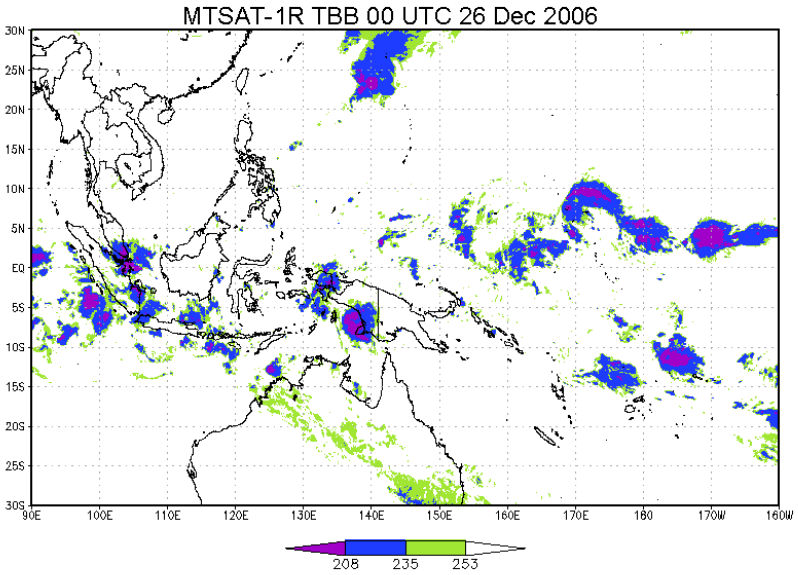
MTSAT-1R TBB 00 UTC 26 Dec 2006
30N
25N
20N
15N
10N
5N
EQ
5S
10S
15S
20S
25S
30S
90E
100E
110E
120E
130E
140E
150E
160E
170E
180
170W
160W
208
235
253

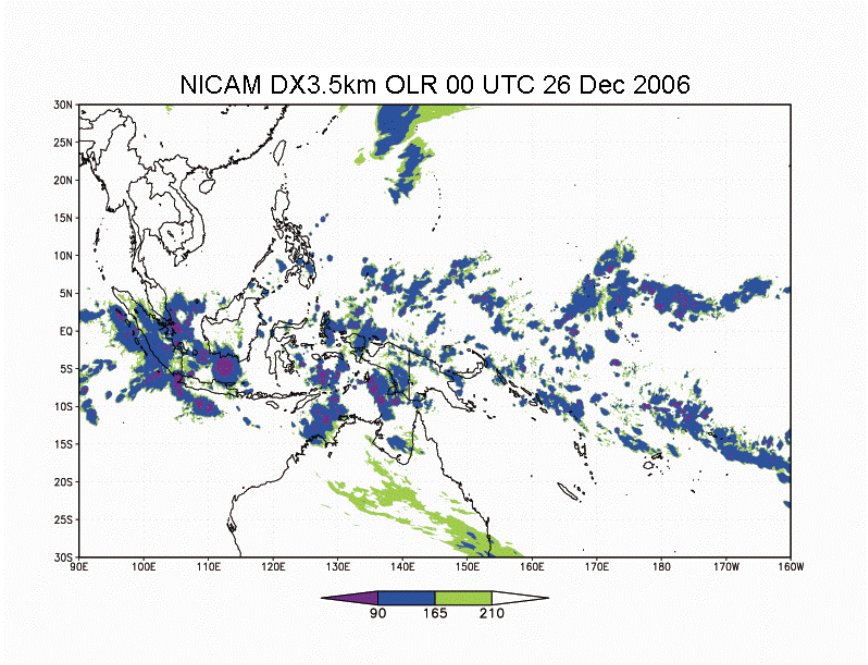
NICAM DX3.5km OLR 00 UTC 26 Dec 2006
30N
25N
20N
15N
10N
5N
EQ
5S
10S
15S
20S
25S
30S
90E
100E
110E
120E
130E
140E
150E
160E
170E
180
170W
160W
90
165
210

Figure 2

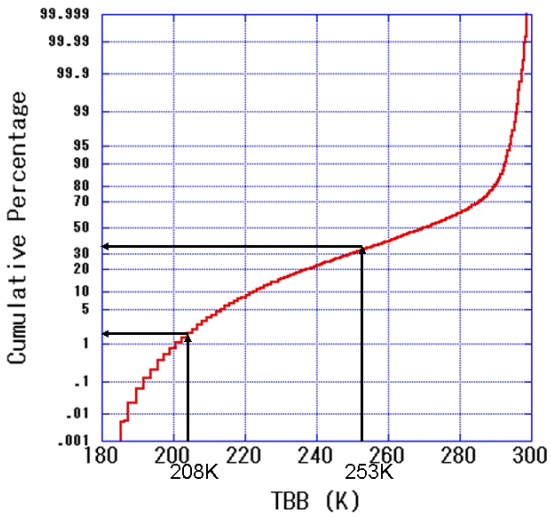
99.999
99.99
99.9
99
95
90
80
70
50
30
20
10
5
1
.1
.01
.001
Cumulative Percentage
180
200
220
240
260
280
300
208K
253K
TBB (K)

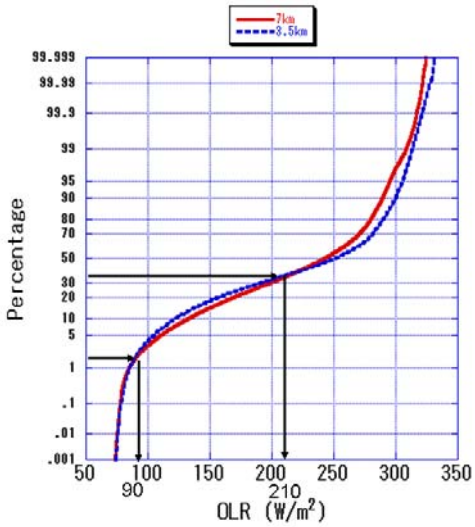
7km
3.5km
99.999
99.99
99.9
99
95
90
80
70
50
30
20
10
5
1
.1
.01
.001
Percentage
50
100
150
200
250
300
350
90
210
OLR (W/m²)

Figure 3

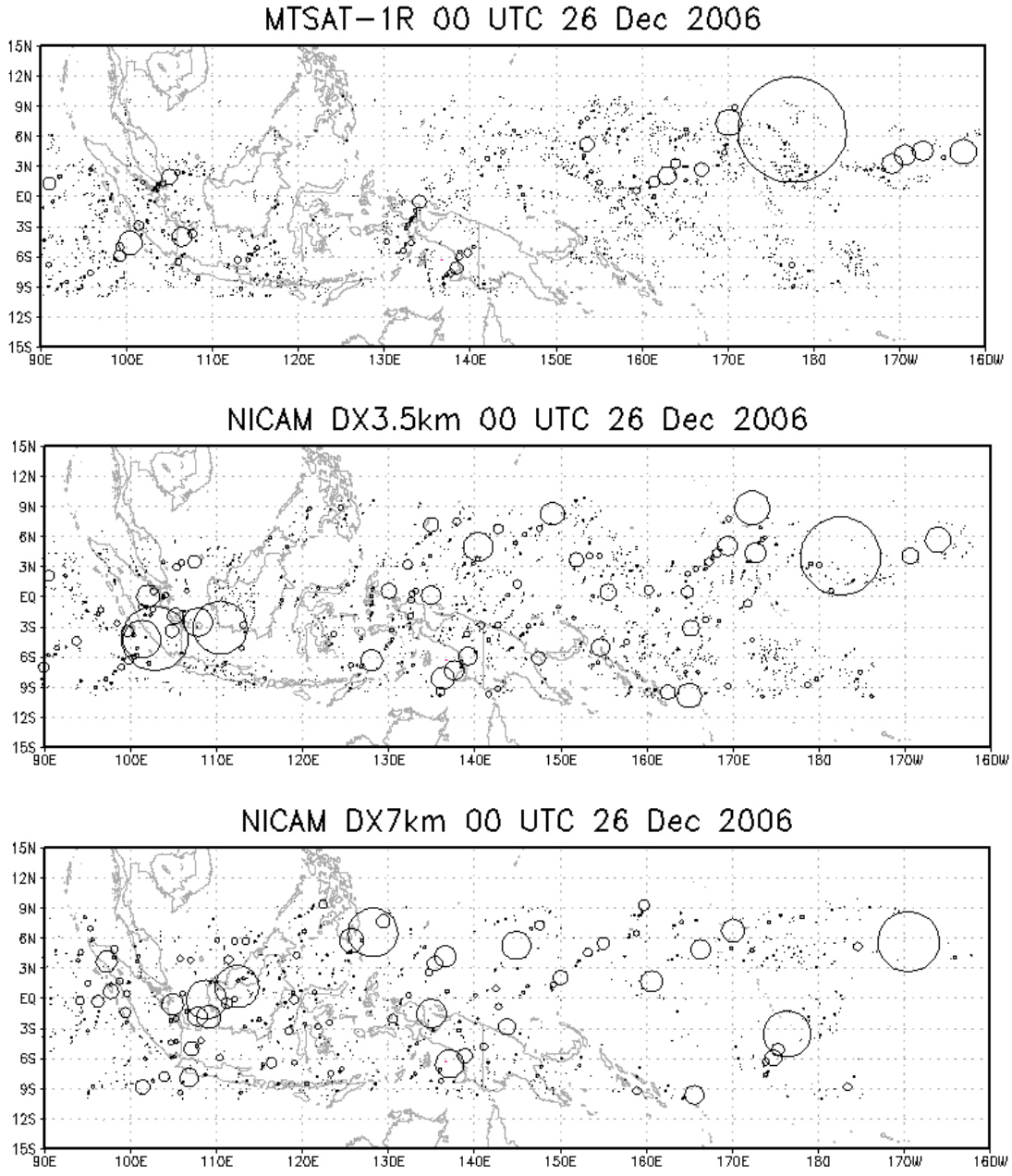
MTSAT−1R 00 UTC 26 Dec 2006
NICAM DX3.5km 00 UTC 26 Dec 2006
NICAM DX7km 00 UTC 26 Dec 2006
15N
12N
9N
6N
3N
EQ
3S
6S
9S
12S
15S
90E
100E
110E
120E
130E
140E
150E
160E
170E
180
170W
160W

Figure 4

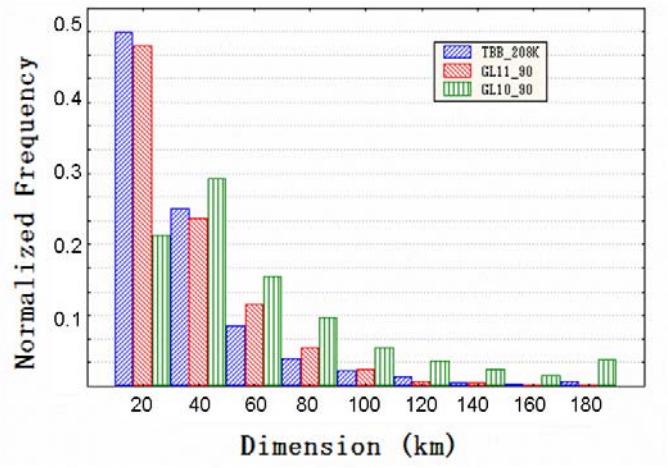
Normalized Frequency
0.5
0.4
0.3
0.2
0.1
TBB_208K
GL11_90
GL10_90
20 40 60 80 100 120 140 160 180
Dimension (km)

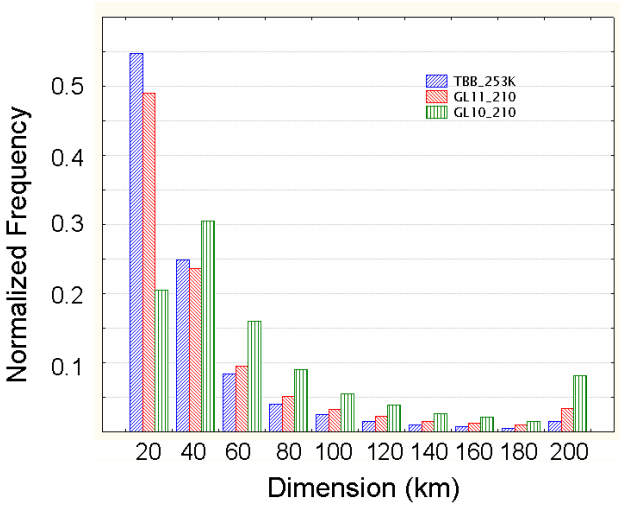
Normalized Frequency
0.5
0.4
0.3
0.2
0.1
TBB_253K
GL11_210
GL10_210
20 40 60 80 100 120 140 160 180 200
Dimension (km)

Figure 5

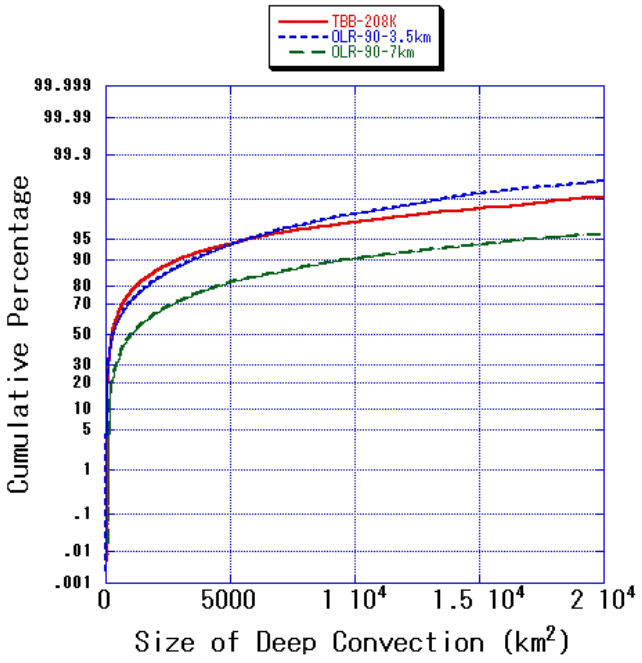
TBB-208K
OLR-90-3.5km
OLR-90-7km
Cumulative Percentage
99.999
99.99
99.9
99
95
90
80
70
50
30
20
10
5
1
.1
.01
.001
0
5000
1 10^4
1.5 10^4
2 10^4
Size of Deep Convection (km^2)

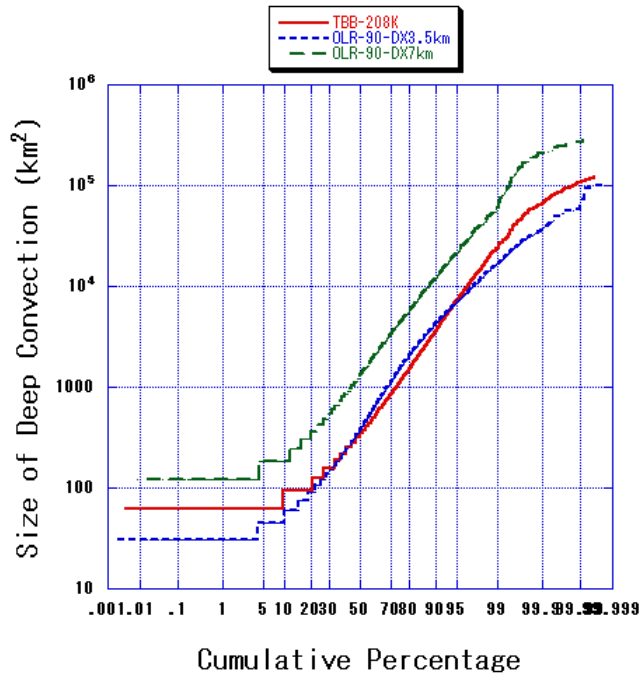
TBB-208K
OLR-90-DX3.5km
OLR-90-DX7km
Size of Deep Convection (km^2)
10^6
10^5
10^4
1000
100
10
.001.01 .1 1 5 10 20 30 50 70 80 90 95 99 99.9 99.99 99.999
Cumulative Percentage

Figure 6

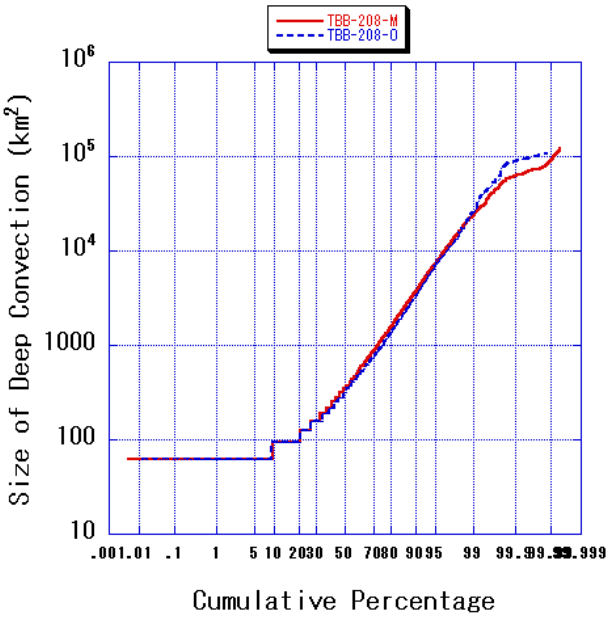
TBB-208-M
TBB-208-O
Size of Deep Convection (km²)
10⁶
10⁵
10⁴
1000
100
10
.001 .01 .1 1 5 10 20 30 50 70 80 90 95 99 99.9 99.99 99.999
Cumulative Percentage

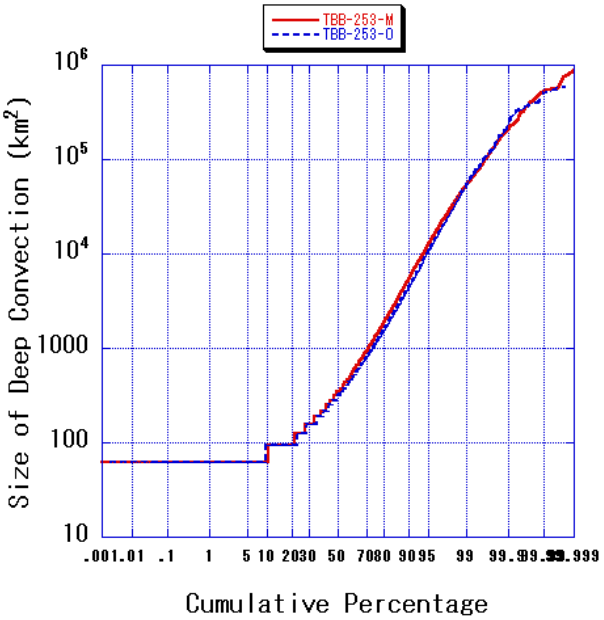
TBB-253-M
TBB-253-O
Size of Deep Convection (km²)
10⁶
10⁵
10⁴
1000
100
10
.001 .01 .1 1 5 10 20 30 50 70 80 90 95 99 99.9 99.99 99.999
Cumulative Percentage

Figure 7

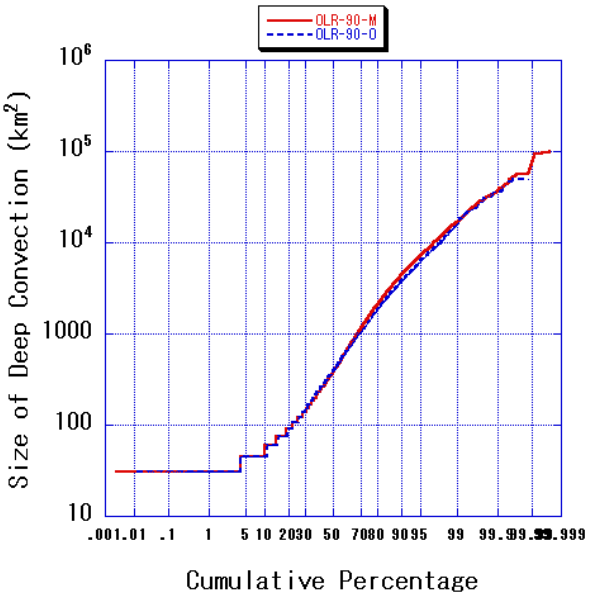
OLR-90-M
OLR-90-O
Size of Deep Convection (km²)
10⁶
10⁵
10⁴
1000
100
10
.001.01 .1 1 5 10 20 30 50 70 80 90 95 99 99.9 99.99 99.999
Cumulative Percentage

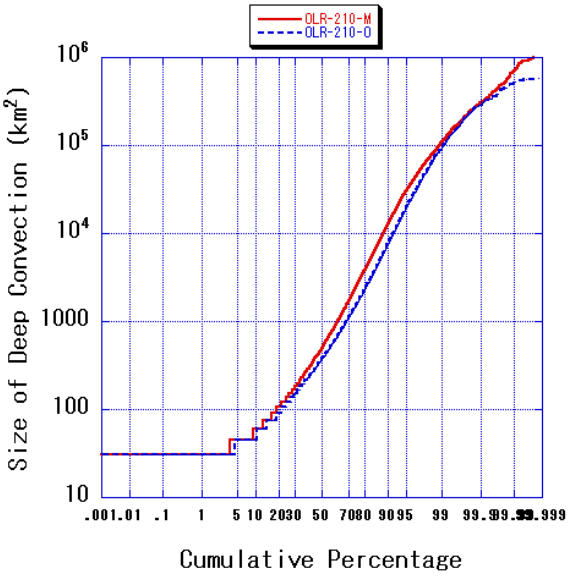
OLR-210-M
OLR-210-O
Size of Deep Convection (km²)
10⁶
10⁵
10⁴
1000
100
10
.001.01 .1 1 5 10 20 30 50 70 80 90 95 99 99.9 99.99 99.999
Cumulative Percentage

Figure 8

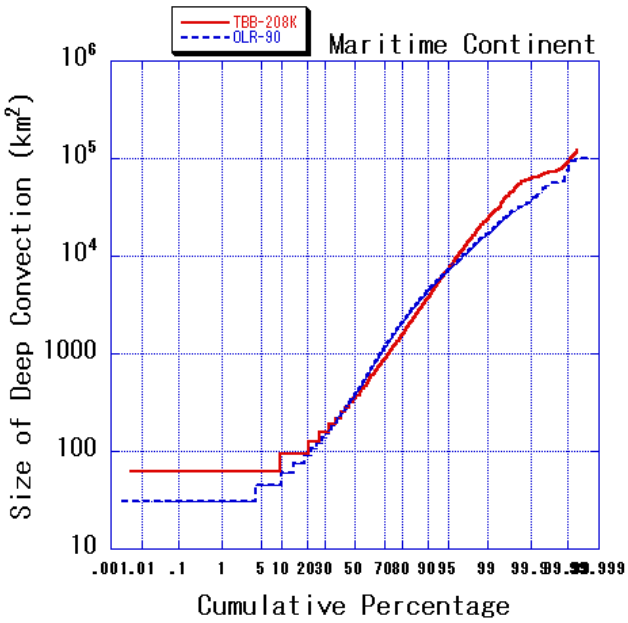
TBB-208K
OLR-90
Maritime Continent
Size of Deep Convection (km²)
10⁶
10⁵
10⁴
1000
100
10
.001.01 .1 1 5 10 20 30 50 70 80 90 95 99 99.9 99.99 99.999
Cumulative Percentage

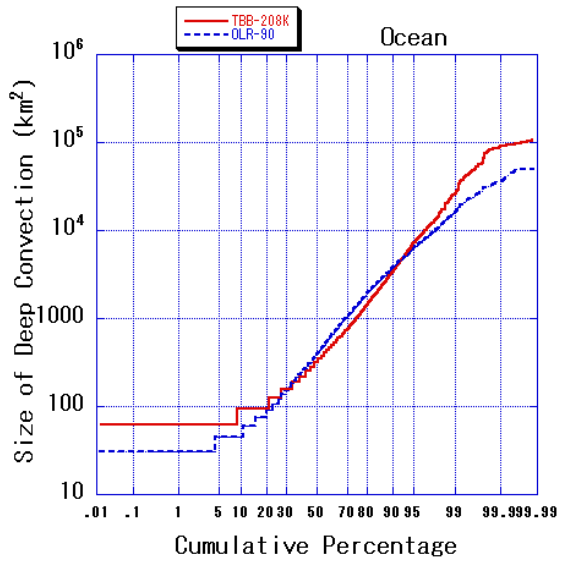
TBB-208K
OLR-90
Ocean
Size of Deep Convection (km²)
10⁶
10⁵
10⁴
1000
100
10
.01 .1 1 5 10 20 30 50 70 80 90 95 99 99.9 99.99
Cumulative Percentage

Figure 9

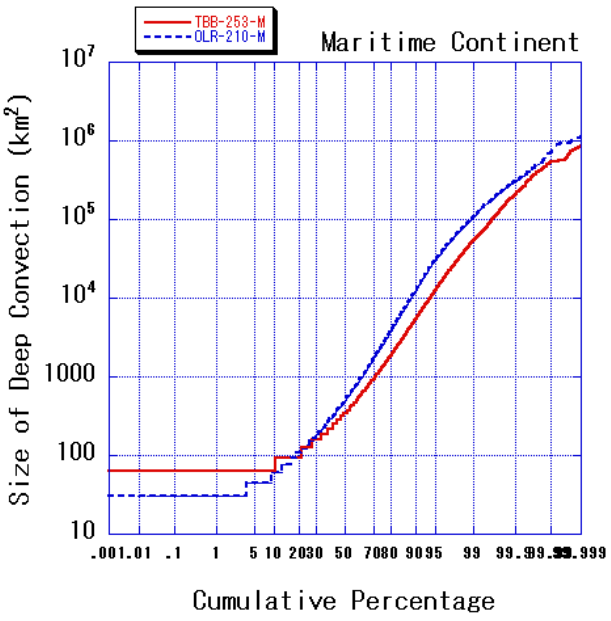
TBB-253-M
OLR-210-M
Maritime Continent
Size of Deep Convection (km²)
10⁷
10⁶
10⁵
10⁴
1000
100
10
.001 .01 .1 1 5 10 20 30 50 70 80 90 95 99 99.9 99.99 99.999
Cumulative Percentage

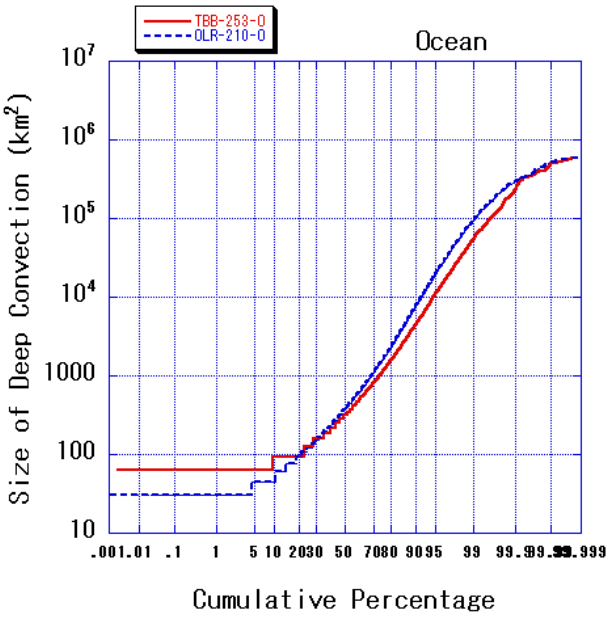
TBB-253-O
OLR-210-O
Ocean
Size of Deep Convection (km²)
10⁷
10⁶
10⁵
10⁴
1000
100
10
.001 .01 .1 1 5 10 20 30 50 70 80 90 95 99 99.9 99.99 99.999
Cumulative Percentage

Figure 10

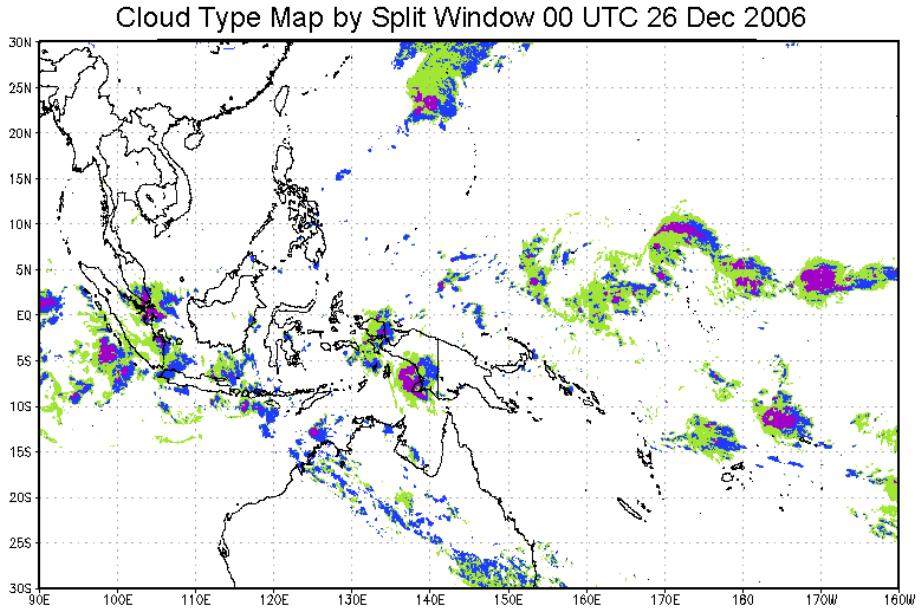
Cloud Type Map by Split Window 00 UTC 26 Dec 2006
30N
25N
20N
15N
10N
5N
EQ
5S
10S
15S
20S
25S
30S
90E
100E
110E
120E
130E
140E
150E
160E
170E
180
170W
160W

Figure 11

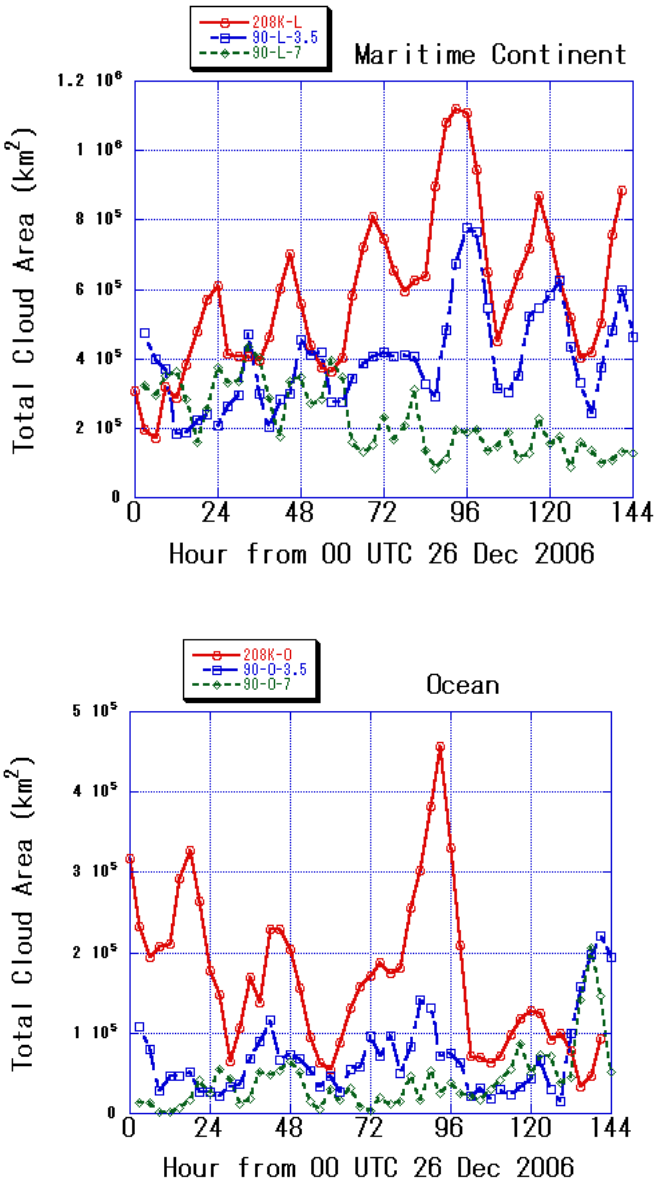
208K-L
90-L-3.5
90-L-7
Maritime Continent
Total Cloud Area (km2)
1.2 10^6
1 10^6
8 10^5
6 10^5
4 10^5
2 10^5
0
0
24
48
72
96
120
144
Hour from 00 UTC 26 Dec 2006
208K-O
90-O-3.5
90-O-7
Ocean
Total Cloud Area (km2)
5 10^5
4 10^5
3 10^5
2 10^5
1 10^5
0
0
24
48
72
96
120
144
Hour from 00 UTC 26 Dec 2006

Figure 12

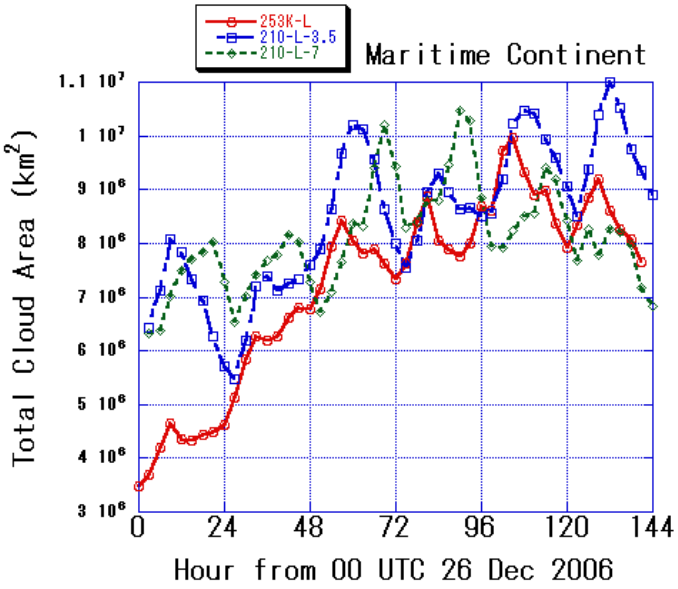
253K-L
210-L-3.5
210-L-7
Maritime Continent
Total Cloud Area (km2)
1.1 10^7
1 10^7
9 10^6
8 10^6
7 10^6
6 10^6
5 10^6
4 10^6
3 10^6
0
24
48
72
96
120
144
Hour from 00 UTC 26 Dec 2006

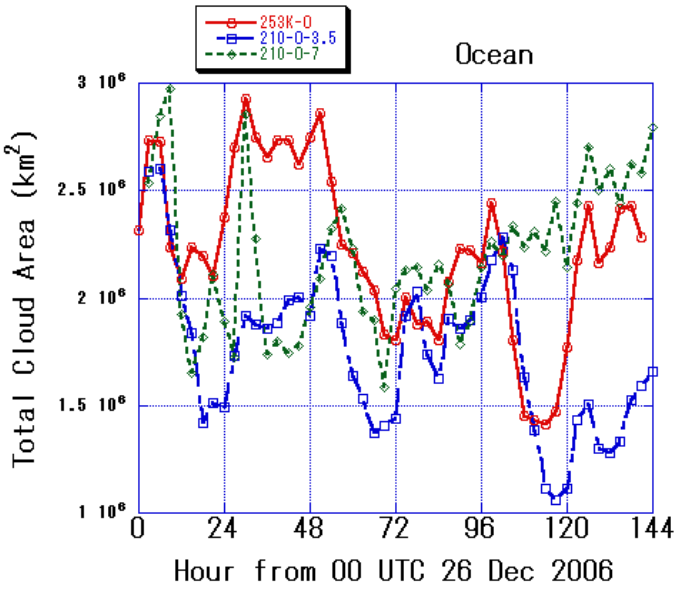
253K-O
210-O-3.5
210-O-7
Ocean
Total Cloud Area (km2)
3 10^6
2.5 10^6
2 10^6
1.5 10^6
1 10^6
0
24
48
72
96
120
144
Hour from 00 UTC 26 Dec 2006

Figure 13

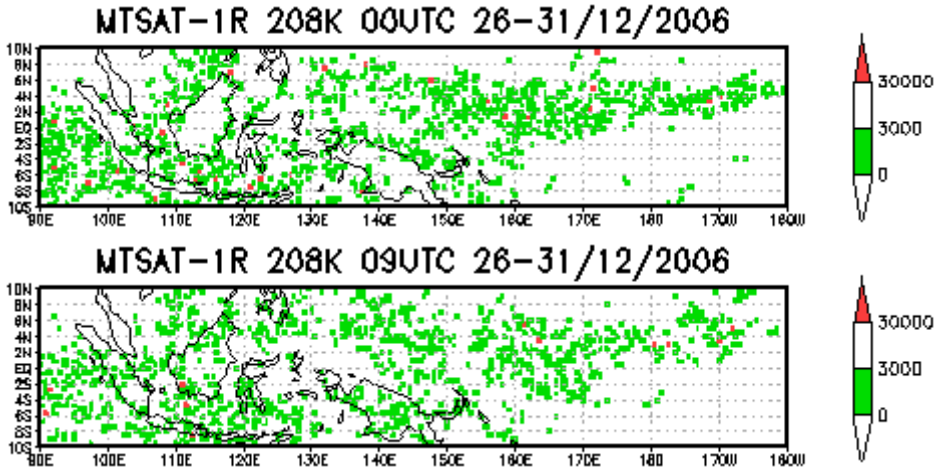
MTSAT-1R 208K 00UTC 26-31/12/2006
MTSAT-1R 208K 09UTC 26-31/12/2006
30000
3000
0
30000
3000
0

Figure 14

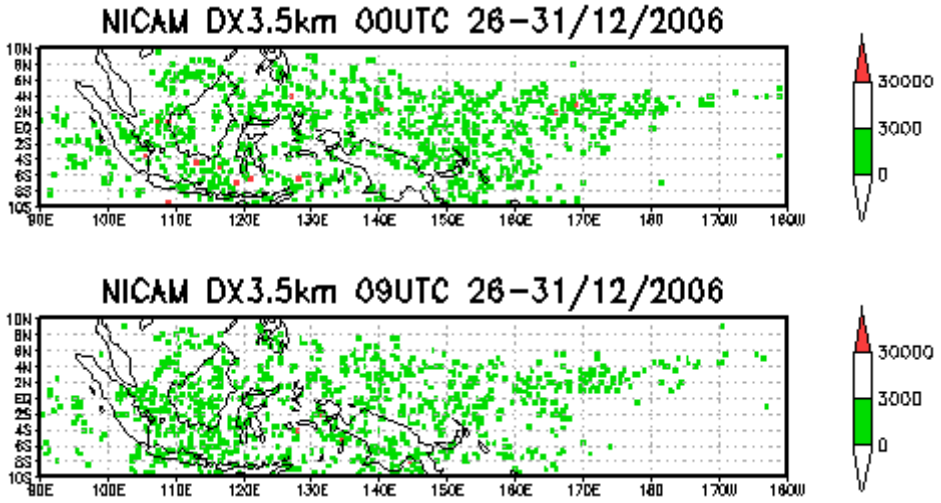
NICAM DX3.5km 00UTC 26-31/12/2006
10N
8N
6N
4N
2N
EQ
2S
4S
6S
8S
10S
90E
100E
110E
120E
130E
140E
150E
160E
170E
180
170W
160W
30000
3000
0
NICAM DX3.5km 09UTC 26-31/12/2006
10N
8N
6N
4N
2N
EQ
2S
4S
6S
8S
10S
90E
100E
110E
120E
130E
140E
150E
160E
170E
180
170W
160W
30000
3000
0

Figure 15